Phase-Based Registration of Cardiac Tagged MR Images by Incorporating Anatomical Constraints

Yitian Zhou[1,3](✉), Mathieu De Craene[1],
Maxime Sermesant[2], and Olivier Bernard[3]

[1] Philips Research Medisys, Suresnes, France
`yitian.zhou@philips.com`
[2] Inria, Asclepios Research Project, Sophia Antipolis, France
[3] CREATIS, CNRS UMR5220, Inserm U1044, INSA-Lyon,
Université Lyon 1, Villeurbanne, France

Abstract. This paper presents a novel method that combines respective benefits of the tracking-based methods and the Gabor-based non-tracking approaches for improving the motion/strain quantification from tagged MR images. The "tag number constant" concept used in Gabor-based non-tracking methods is integrated into a recent phase-based registration framework. We evaluated our method on both synthetic and real data: (1) on a synthetic data of a normal heart, we found that the constraint improved both longitudinal and circumferential strains accuracies; (2) on 15 healthy volunteers, the proposed method achieved better tracking accuracy compared to three state-of-the-art methods; (3) on one patient dataset, we show that our method is able to distinguish the infarcted segments from the normal ones.

Keywords: Cardiac tagged MR · Strain · Tag number constant constraint

1 Introduction

The quantification of regional myocardial motion and strains remains a central challenge for diagnosing heart diseases. Tagged magnetic resonance imaging (TMRI) is currently the gold standard for quantifying local myocardial deformations. The underlying technique is based on the creation of non-invasive magnetic markers (tags) that move with the myocardium over the cardiac cycle. Tracking these tags permits the recovery of underlying cardiac deformations.

As for the state-of-the-art on cardiac motion tracking from TMRI, the reader is referred to [1] for a thorough analysis. We provide here a brief discussion relevant to this paper. All the developed algorithms can be roughly classified into two categories: the tracking-based and the Gabor-based non-tracking methods. The tracking-based methods consist in (1) tracking the myocardial motion by HARP [2], optical flow or any other non-rigid registration technique and (2) deriving the strain from the tracked field. One limitation of such methods is that

T. Mansi et al. (Eds.): STACOM 2016, LNCS 10124, pp. 39–47, 2017.
DOI: 10.1007/978-3-319-52718-5_5

the computed strain is highly sensitive to the regularization parameter used for the tracking [3]. As a result, Qian *et al.* [3], Bruurmijn *et al.* [4] and Kause *et al.* [5] opted for bypassing the tracking issue. They proposed to directly compute Eulerian strain maps from spatial tag frequencies that were filtered out by Gabor filters. The idea is that temporal variations in spatial tag frequencies reveals the stretch/shortening of the myocardium. For example, an increased spatial tag frequency means that the tissue undergoes a local contraction. All of the above groups made use of this concept to compute the deformation gradient tensor which is further related to strain. They all used the assumption that the **N**umber of **T**ags between two myocardial points remains **C**onstant over the cardiac cycle (denoted as NTC hereinafter). This assumption is implicit in [3] while explicit in both [4,5]. The authors claim that it makes their strain estimate independent to any tracking field. However, they overlook that a tracking is always required for reporting strain evolution at all time points per material point, which is of clinical importance in diagnosing heart diseases like dyssynchrony, infarction *etc.*

In this paper, we propose to integrate the NTC into a recent phase-based registration framework [6]. By exploiting NTC as constraints defined in the anatomical directions of the heart, we aim to reduce the dependency of the strain output to the amount of regularization and report strain curves per material point. The constraints are used as an additional step for refining the tracking of myocardial points located in the middle of the myocardium. The role the NTC plays in improving the quantification is evaluated on both synthetic and real data.

2 Data Acquisition and Preprocessing

A full description of the acquisition of the TMRI used can be found in [1]. The data consists of three sequences with orthogonal tagging directions. In the following, the sequence is identified by the index k ($k = 0, 1, 2$).

We follow the preprocessing steps described in [1]. It consists of (1) the computation of HARP phase; (2) the manual segmentation of the left ventricle (LV) at end-diastole and its resampling to a volumetric mesh. The resampled mesh has three layers in the radial direction: endocardium (endo), epicardium (epi) and a middle layer located between them (mid); and (3) the division of LV domain into local windows according to the AHA standard. The apex segment (n$^{\text{o}}$ 17) was further subdivided into three equal parts, resulting in 19 windows in total. Gaussian window functions (Fig. 2(b)) were then defined for each window.

3 Methodology

We chose to track each of the endo/mid/epi layers independently (This choice is justified later in Sect. 3.1). First, we track each of the endo/epi/mid layers by the purely phase-based registration (Sect. 3.2) using a recent parametric motion model (Sect. 3.1). Second, we refine the motion of the mid layer using the phase-based registration with NTC constraints (Sect. 3.3). We chose not to refine the endo and epi layers because they subject to tracking artifacts which impact the computation of accurate number of tags that we impose as constraints. The way we implement the NTC constraint is later detailed in Sect. 3.3.

3.1 Motion Model

We use the parametric model proposed in [1] to represent the motion. With the acquisition protocol used, there is a poor tag resolution in the radial direction (only 2 or 3 line tags), making it difficult to capture accurate transmural motion variations [1]. As a result, we decided to remove the three parameters that represent the transmural gradients of *Rad.*, *Long.* and *Circ.* (RLC) displacements from the model. This leads to a 9-parameter model per window per layer:

$$\begin{aligned}
&\mathbf{v}(\mathbf{x}) = \sum_i \varphi^{(i)}(\mathbf{x})\mathbf{v}^{(i)}(\mathbf{x}) \\
&\text{with } \mathbf{v}^{(i)}(\mathbf{x}) = \big(a_{rl}^{(i)} l^{(i)}(\mathbf{x}) + a_{rc}^{(i)} c^{(i)}(\mathbf{x}) + b_r^{(i)}\big)\hat{\mathbf{e}}_r(\mathbf{x}) + \\
&\qquad\qquad\quad \big(a_{ll}^{(i)} l^{(i)}(\mathbf{x}) + a_{lc}^{(i)} c^{(i)}(\mathbf{x}) + b_l^{(i)}\big)\hat{\mathbf{e}}_l(\mathbf{x}) + \\
&\qquad\qquad\quad \big(a_{cl}^{(i)} l^{(i)}(\mathbf{x}) + a_{cc}^{(i)} c^{(i)}(\mathbf{x}) + b_c^{(i)}\big)\rho(\mathbf{x})\hat{\mathbf{e}}_c(\mathbf{x})
\end{aligned} \tag{1}$$

where $\mathbf{v}^{(i)}$ is the local motion inside the window i, $\varphi^{(i)}$ are Gaussian window functions, and $\mathbf{v}$ is the global motion that results from mixing local motions. $\hat{\mathbf{e}}_d(\mathbf{x})$ $(d = r, l, c)$ are RLC directions. $l^{(i)}$ and $c^{(i)}$ are local coordinates along *Long.* and *Circ.* directions respectively. ρ is the distance to the long axis [1]. In this way, $\{b_r^{(i)}, b_l^{(i)}, b_c^{(i)}\}$ represent translations, $\{a_{ll}^{(i)}, a_{cc}^{(i)}\}$ are *Long.* and *Circ.* strains, and $\{a_{lc}^{(i)}, a_{cl}^{(i)}\}$ are *Long.* - *Circ.* shearings. $\{a_{rl}^{(i)}, a_{rc}^{(i)}\}$ are *Rad.* displacement gradients in *Long.* and *Circ.* directions (not transmural). We then have 9×19 parameters for modeling the motion of each of the endo/mid/epi layers.

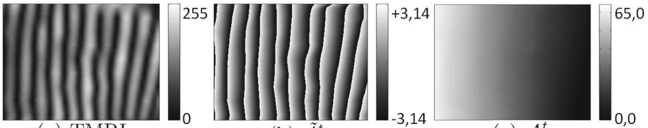

(a) TMRI (b) $\tilde{\mathcal{A}}_k^t$ (c) $\mathcal{A}_k^t$

Fig. 1. Illustration of (a) the TMRI image, (b) the HARP phase, (c) the unwrapped phase computed taking a pixel's phase value as reference.

3.2 Phase-Based Registration *Without* Constraint

We aim to optimize the motion $\mathbf{v}$ according to phase-based SSD [6]:

$$E_{phase}(\mathbf{v}) = \int_{\Omega} \sum_{k=0}^{2} \omega_k(\mathbf{x}, \mathbf{u}(\mathbf{x}))\big(\mathcal{A}_k^{ref}(\mathbf{x}) - \mathcal{A}_k^t(\mathbf{x} + \mathbf{u}(\mathbf{x}) + \mathbf{v}(\mathbf{x})\big)^2 d\mathbf{x} \tag{2}$$

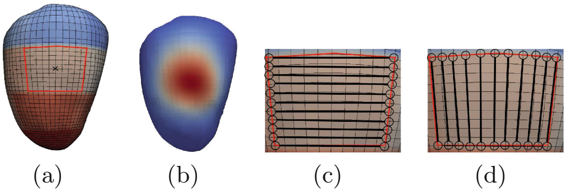

Fig. 2. The surface layer mesh with windows and the definition of control point pairs. (a): LV mesh and windows; (b): the window function $\varphi^{(i)}(\mathbf{x})$; (c), (d) show respectively the control point pairs in *Circ.* and *Long.* directions.

Where k indicates the sequence, and ref indicates the reference time (the last frame in our case). $\mathcal{A}_k^t$ is the unwrapped phase as is illustrated in Fig. 1. We use the unwrapped phase for the formulation because it facilitates the computation of tag numbers which will be described later in Sect. 3.3. Both $\mathbf{u}$ and $\mathbf{v}$ are motions from *ref* to t. $\mathbf{u}$ is the current motion which is known, while $\mathbf{v}$ is the motion model in Eq. 1. We opt for registering all other frames to *ref* for avoiding the accumulation of errors during the tracking. ω_k is a weight function introduced in [6]. The reader is referred to [6] for more details.

3.3 Phase-Based Registration *With* Constraint

In this section, we describe how to implement the NTC for refining the motion. It is rather intuitive that the number of tags between two material points remains unchanged throughout the cardiac cycle. As a consequence, we propose to add an additional constraint energy to Eq. 2 for penalizing the deviation of tag numbers to that at *ref*.

First, we select a number of myocardial point pairs following the *circ.* and *long.* directions as shown in Fig. 2(c) and (d). For each window, the boundary mesh nodes are paired in *circ.* and *long.* directions. Those node pairs are chosen for defining the constraint. We take all such point pairs from the mid-level and apical windows. Those from the basal windows are excluded because segmentation errors are more severe [1]. We denote these point pairs by $(\mathbf{p}_j, \mathbf{q}_j)$ with $j = 0$ to $\mathcal{J} - 1$ where $\mathbf{p}_j$ and $\mathbf{q}_j$ are the material coordinates at *ref* time.

The number of tag between $\mathbf{p}_j$ and $\mathbf{q}_j$ is then computed by normalizing their unwrapped phase difference by 2π. The constraint energy is defined as follows:

$$\begin{aligned} E_c(\mathbf{v}) &= \sum_{j=0}^{\mathcal{J}-1} \sum_{k=0}^{2} \left(\frac{1}{2\pi} \mathcal{D}_{k,j}^{ref} - \frac{1}{2\pi} \mathcal{D}_{k,j}^{t} \right)^2 \\ \text{with} \quad & \mathcal{D}_{k,j}^{ref} = \mathcal{A}_k^{ref}(\mathbf{q}_j) - \mathcal{A}_k^{ref}(\mathbf{p}_j) \\ & \mathcal{D}_{k,j}^{t} = \mathcal{A}_k^{t}(\mathcal{T}_u(\mathbf{q}_j) + \mathbf{v}(\mathbf{q}_j)) - \mathcal{A}_k^{t}(\mathcal{T}_u(\mathbf{p}_j) + \mathbf{v}(\mathbf{p}_j)) \\ & \mathcal{T}_u(\mathbf{x}) = \mathbf{x} + \mathbf{u}(\mathbf{x}) \end{aligned} \tag{3}$$

where $\mathbf{u}$ has the same definition as that in Eq. 2 and $\mathbf{v}$ is given by Eq. 1.

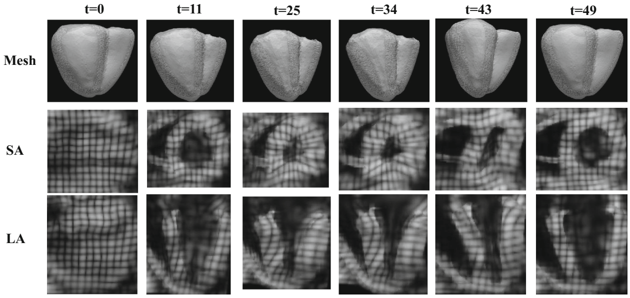

Fig. 3. Ground truth meshes, short- and long- axis slices of the synthetic TMRI (three sequences of line taggings are multiplied for better visualization).

E_c can be decomposed into a number of local quadratic forms. Actually, it is upper-bounded by the sum of those quadratic forms. The reader is referred to the appendix for more details on the derivation of the following equation:

$$E_c(\mathbf{v}) \leq \sum_i E_c^{(i)}(\mathbf{v}^{(i)}) \tag{4}$$

where i indicates the window, $\mathbf{v}^{(i)}$ is the local motion described in Eq. 1, and $E_c^{(i)}$ is the local quadratic form corresponding to the window i.

Similarly for $E_{phase}(\mathbf{v})$, we have $E_{phase}(\mathbf{v}) \leq \sum_i E_{phase}^{(i)}(\mathbf{v}^{(i)})$ with $E_{phase}^{(i)}$ being local quadratic forms according to [6]. Finally, by combining the phase-based term E_{phase} and the constraint energy E_c, we have E defined as:

$$E(\mathbf{v}) = E_{phase}(\mathbf{v}) + \lambda\xi E_c(\mathbf{v}) \leq \sum_i \left(E_{phase}^{(i)}(\mathbf{v}^{(i)}) + \lambda\xi E_c^{(i)}(\mathbf{v}^{(i)})\right) \tag{5}$$

Where ξ is a normalizing factor. We set it to 10^3 empirically in our experiments. λ is the weight of the constraint. It is tuned later in Sect. 5.1. Equation 5 means that E is upbounded by the sum of local energies $E_{phase}^{(i)} + \lambda\xi E_c^{(i)}$. E is minimized by optimizing each of the local quadratic form through solving a linear system. The whole process is iterated until convergence.

4 Generation of Synthetic Images

We combined a real 3D TMRI recording denoted as $\mathcal{I}_k^t$ and an electro-mechanical (E/M) model simulating the cardiac electrophysiological activation and the myocardial contraction [8] for generating synthetic images.

It consists of four steps: (1) we track the LV in the real recording by [1]. The output is a sequence of volumetric meshes denoted as $\mathcal{M}^t$; (2) we use the E/M model to simulate myocardial deformations corresponding to the LV geometry $\mathcal{M}^0$, leading to another sequence of meshes $\mathcal{S}^t$; (3) since $\mathcal{M}^0$ and $\mathcal{S}^0$ are equivalent, it is easy to build a Thin Plate Spline (TPS) transformation that warps the real images $\mathcal{I}_k^t$ to the simulation $\mathcal{S}^t$; and (4) we correct the apparent motion extracted in (1) by transformations contained in $\mathcal{S}^t$ sequence so that the motion in the simulated images corresponds to the E/M model. Each myocardial voxel position at time t is mapped back to the first frame. The new intensity is then computed by linearly interpolating $\mathcal{I}_k^0$. In this study, we simulated a synthetic data for a normal heart shown in Fig. 3. The spatial resolution is $0.96 \times 0.96 \times 7.71\,mm$ and line tag spacing is $7\,mm$.

5 Result

5.1 Synthetic Data

We use the synthetic data for tuning the constraint weight λ (Eq. 5) and investigating whether the constraint helps improving strain accuracy. Here the evaluation only involves the mid layer where the constraint was used. We display in Fig. 4(a) the evolution of RMSE motion errors at end-systole with λ. From the result, we observe that there is an optimal value around $\lambda = 1.5$. We then compared the performance between using $\lambda = 0$ and $\lambda = 1.5$ on strain quantification in Fig. 4(b) and (c). We used the Engineering strain as described in [1]. We see that for both strains, using the constraint gives smaller RMSE strain errors. This confirms the interest of utilizing the NTC constraint.

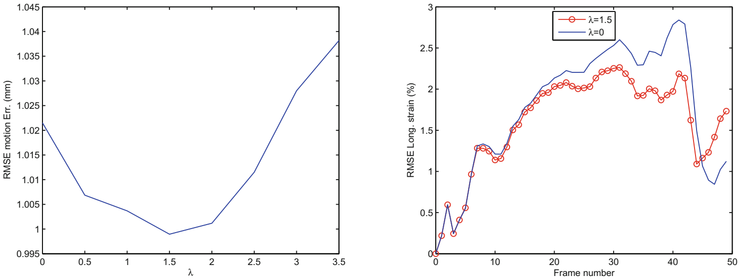

(a) Tuning λ (b) Long. strain

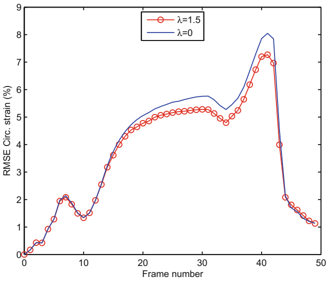

(c) Circ. strain

Fig. 4. (a):Evolution of motion errors at end-systole with the constraint energy weight λ; (b): Temporal evolution of Long. and (c): Circ. strain errors.

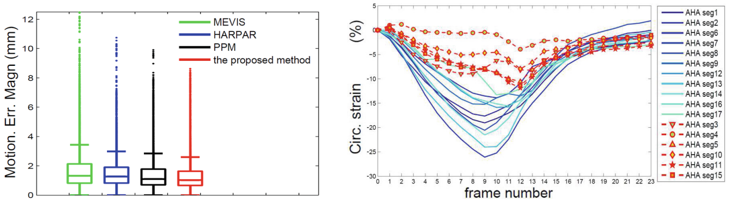

(a) healthy volunteers (b) a patient with infarction

Fig. 5. (a): Volunteer data landmark tracking errors using $\lambda = 1.5$ compared to the state-of-the-art; (b) Circ. strain curves on a patient with fibrosis. Solid lines show normal segments while curves with markers show segments with fibrosis.

5.2 Real Data

We also evaluated our method on 15 healthy volunteer datasets which are publicly available from [9]. Each volunteer data has 24 manually tracked landmarks located in the basal, mid and apical myocardium. These landmarks were warped forward in time by computing barycentric coordinates in the first frame and propagating them through the sequence of volumetric meshes. From Fig. 5(a), we see that the dispersion of motion errors is reduced when compared to the purely phase-based registration (without NTC constraint) PPM [6]. This result is further confirmed by Levene's test. The returned p-value is below 0.05, rejecting the null hypothesis that their variances are equal. Besides, our method slightly outperformed the other two recent methods HARPAR (regularized HARP) [1] and MEVIS (quadrature-filter based) [9] in both median and variance values.

Moreover, our method was evaluated on a patient who had fibrosis at the entire inferior wall, part of the inferolateral wall and part of the inferoseptal wall (AHA n^{o} 3,4,5,10,11,15) confirmed by late-enhancement MR. In Fig. 5(b) we observe reduced *Circ.* strain values for those infarcted segments, showing a clear discrepancy between normal segments and those with fibrosis.

6 Conclusion and Discussion

This paper integrates the NTC constraints into a recent phase-based registration framework for refining the tracking. On synthetic data, we observe that integrating the constraint improved both motion and strain (*Long.* and *Circ.*) accuracies. On healthy volunteers, the proposed method gives better accuracy compared to three state-of-the-art algorithms. On a patient with infarction, we observe reduced *Circ.*strain values for those AHA segments with fibrosis. We admit that a more thorough validation needs to be done both synthetically and clinically in the future. However, our aim is to show the potential benefits of combining respective advantages of both methods (tracking-based and Gabor-based non-tracking), which we consider as an interesting research field.

Appendix

In Eq. 3, conducting 1^{st}-order approximations on $\mathcal{A}_k^t$ leads to:

$$E_c(\mathbf{v}) \approx \sum_j \sum_k \left(\frac{\mathcal{A}_k^{ref}(\mathbf{q}_j) - \mathcal{A}_k^{ref}(\mathbf{p}_j)}{2\pi} - \frac{\mathcal{A}_k^t(\mathcal{T}_u(\mathbf{q}_j)) - \mathcal{A}_k^t(\mathcal{T}_u(\mathbf{p}_j)) + \delta_k^j(\mathbf{v})}{2\pi} \right)^2 \quad (6)$$
$$\text{with } \delta_k^j(\mathbf{v}) = \nabla\mathcal{A}_k^t(\mathcal{T}_u(\mathbf{q}_j)) \cdot \mathbf{v}(\mathbf{q}_j) - \nabla\mathcal{A}_k^t(\mathcal{T}_u(\mathbf{p}_j)) \cdot \mathbf{v}(\mathbf{p}_j)$$

Instead of computing $\mathcal{A}_k^t$ maps by phase unwrapping which is highly sensitive to image artifacts, we chose to circumvent the issue by (1) computing $\nabla\mathcal{A}_k^t$ from HARP phases by the method described in [2] and (2) further computing $\mathcal{A}_k^\tau(\mathbf{q}_j) - \mathcal{A}_k^\tau(\mathbf{p}_j)$ ($\tau = ref$ and t) by curvilinear integration of $\nabla\mathcal{A}_k^\tau$. The path of integration is easily defined using our mesh topology. Equation 6 then becomes:

$$E_c(\mathbf{v}) = \sum_j \sum_k \left(\beta_k^j - \frac{1}{2\pi}\delta_k^j(\mathbf{v})\right)^2$$
$$\text{with } \beta_k^j = \frac{1}{2\pi}\int_{\mathbf{p}_j}^{\mathbf{q}_j} \nabla\mathcal{A}_k^{ref}(\mathbf{x})d\mathbf{x} - \frac{1}{2\pi}\int_{\mathcal{T}_u(\mathbf{p}_j)}^{\mathcal{T}_u(\mathbf{q}_j)} \nabla\mathcal{A}_k^t(\mathbf{x})d\mathbf{x} \quad (7)$$

where β_k^j is known and $\delta_k^j(\mathbf{v})$ contains the model parameters.

We first replace both $\varphi^{(i)}(\mathbf{p}_j)$ and $\varphi^{(i)}(\mathbf{q}_j)$ in $\delta_k^j(\mathbf{v})$ by $g_j^{(i)} = \frac{\varphi^{(i)}(\mathbf{p}_j)+\varphi^{(i)}(\mathbf{q}_j)}{2}$. This is justified by the fact that $\mathbf{p}_j$ and $\mathbf{q}_j$ are symmetric to the window center (see Fig. 2), thus $\varphi^{(i)}(\mathbf{p}_j) \approx \varphi^{(i)}(\mathbf{q}_j)$. $\delta_k^j(\mathbf{v})$ then becomes:

$$\delta_k^j(\mathbf{v}) \approx \sum_i g_j^{(i)} \mathcal{L}_j^{(i)}(\mathbf{v}^{(i)})$$
$$\text{with } \mathcal{L}_j^{(i)}(\mathbf{v}^{(i)}) = \nabla\mathcal{A}_k^t(\mathcal{T}_u(\mathbf{q}_j)) \cdot \mathbf{v}^{(i)}(\mathbf{q}_j) - \nabla\mathcal{A}_k^t(\mathcal{T}_u(\mathbf{p}_j)) \cdot \mathbf{v}^{(i)}(\mathbf{p}_j) \quad (8)$$

Then, applying the *Partition-of-Unity* property [7] of $g_j^{(i)}$ leads directly to [7]:

$$E_c(\mathbf{v}) \leq \sum_i \sum_j g_j^{(i)} \sum_k \left(\beta_k^j - \frac{1}{2\pi}\mathcal{L}_j^{(i)}(\mathbf{v}^{(i)})\right)^2 = \sum_i E_c^{(i)}(\mathbf{v}^{(i)}) \quad (9)$$

Where $E_c^{(i)}$ is quadratic since $\mathcal{L}_j^{(i)}$ is linear in the motion parameters of $\mathbf{v}^{(i)}$.

References

1. Zhou, Y., Bernard, O., Saloux, E., Manrique, A., Allain, P., Makram-Ebeid, S., De Craene, M.: 3D harmonic phase tracking with anatomical regularization. Med. Image Anal. **26**(1), 70–81 (2015)

2. Osman, N.F., Kerwin, W.S., McVeigh, E.R., Prince, J.L.: Cardiac motion tracking using cine harmonic phase (HARP) magnetic resonance imaging. Magn. Reson. Med. **42**(6), 1048 (1999)
3. Qian, Z., Liu, Q., Metaxas, D.N., Axel, L.: Identifying regional cardiac abnormalities from myocardial strains using nontracking-based strain estimation and spatio-temporal tensor analysis. IEEE Trans. Med. Imaging **30**(12), 2017–2029 (2011)
4. Bruurmijn, L.C.M., Kause, H.B., Filatova, O.G., Duits, R., Fuster, A., Florack, L.M.J., Assen, H.C.: Myocardial deformation from local frequency estimation in tagging MRI. In: Ourselin, S., Rueckert, D., Smith, N. (eds.) FIMH 2013. LNCS, vol. 7945, pp. 284–291. Springer, Heidelberg (2013). doi:10.1007/978-3-642-38899-6_34
5. Kause, H.B., Filatova, O.G., Duits, R., Bruurmijn, L.C.M., Fuster, A., Westenberg, J.J.M., Florack, L.M.J., van Assen, H.C.: Direct myocardial strain assessment from frequency estimation in tagging MRI. In: Camara, O., Mansi, T., Pop, M., Rhode, K., Sermesant, M., Young, A. (eds.) STACOM 2013. LNCS, vol. 8330, pp. 212–219. Springer, Heidelberg (2014). doi:10.1007/978-3-642-54268-8_25
6. Zhou, Y., De Craene, M., Bernard, O.: Phase-based registration of cardiac tagged mr images using anatomical deformation model. In: 2016 IEEE 13th International Symposium on Biomedical Imaging (ISBI), pp. 617–620. IEEE (2016)
7. Makram-Ebeid, S., Somphone, O.: Non-rigid image registration using a hierarchical partition of unity finite element method. In: 2007 IEEE 11th International Conference on Computer Vision ICCV 2007, pp. 1–8. IEEE (2007)
8. Marchesseau, S., Delingette, H., Sermesant, M., Ayache, N.: Fast parameter calibration of a cardiac electromechanical model from medical images based on the unscented transform. Biomech. Model. Mechanobiol. **12**(4), 815–831 (2013)
9. Tobon-Gomez, C., De Craene, M., Mcleod, K., Tautz, L., Shi, W., Hennemuth, A., Prakosa, A., Wang, H., Carr-White, G., Kapetanakis, S., et al.: Benchmarking framework for myocardial tracking and deformation algorithms: An open access database. Med. Image Anal. **17**(6), 632–648 (2013)